Direct-forcing fictitious domain method for simulating non-Brownian active particles

Zhaowu Lin and Tong Gao

Phys. Rev. E **100**, 013304 — Published 8 July 2019

DOI: 10.1103/PhysRevE.100.013304

A direct-forcing fictitious domain method for simulating non-Brownian active particles

Zhaowu Lin[1] and Tong Gao[1,2*]

[1] *Department of Mechanical Engineering*
[2] *Department of Computational Mathematics, Science and Engineering*
Michigan State University

(Dated: June 24, 2019)

We present a direct-forcing fictitious domain method for simulating non-Brownian Squirmer particles with both the hydrodynamic interactions and collisions being fully resolved. In this method, we solve the particle motion by distributing collocation points inside the particle interior domain that overlay upon a fixed Eulerian mesh. The fluid motions, including those of the "fictitious fluids" being extended into the particle, are solved on the entire computation domain. Pseudo body forces are used to enforce the fictitious fluids to follow the particle movement. A direct forcing approach is employed to map physical variables between the overlaid meshes, which does not require additional iterations to achieve convergence. We perform a series of numerical studies at both small and finite Reynolds numbers. First of all, accuracy of the algorithm is examined in studying benchmark problems of a free-swimming Squirmer and two side-by-side Squirmers. Then we investigate statistic properties of the quasi-2D collective dynamics for a monolayer of Squirmer particles that are confined on a surface immersed in a bulk flow. Finally, we explore the physical mechanisms of how a freely-moving short cylinder interacts with a monolayer of active particles, and find out that the cylinder movement is dominated by collision. We demonstrate that a more directional migration of cylinder can be resultant from an inhomogeneous distribution of active particles around the cylinder that has an anisotropic shape.

I. INTRODUCTION

There has been an increasing interest during the past decade in exploring non-equilibrium physics of "wet" active matter systems where suspended self-driven microparticles move collectively, featuring fascinating pattern formation, non-equilibrium order transitions, anomalous fluctuations and mechanical properties [1]. Examples include bacterial swarms [2, 3], collections of synthetic colloidal particles [4, 5], and mixtures of cytoskeletal filaments driven by molecular motors [6]. In these systems, the motile microswimmers exert forces upon the ambient liquid which itself provides a coupling medium for generation of complex dynamics.

Modeling and simulation of active matter is challenging due to the multiscale nature of the underlying unstable dynamics. Earlier theoretical studies have investigated several aspects of active matter systems at different scales, from the dynamics and mechanical properties of single particle motion to the macroscopic behavior and stability of active suspensions [1, 7–10]. While continuum models have been successfully used in capturing collective behaviors that are qualitatively similar to experimental observations, these models often rely on assumptions of specific geometries (e.g., spherical, rod-like), as well as mono-dispersed shape and homogeneous particle distribution [11–17]. Alternatively, particle-based simulations [3, 18, 19] can represent microscopic interactions in detail, their computational costs typically limit cross-scale studies when both long-ranged (e.g., hydrodynamic) and short-ranged (steric interactions, contact, etc.) need to be resolved simultaneously for

*Electronic address: gaotong@egr.msu.edu

a large number of particles.

Numerous numerical methods have been developed to solve small particle motion in viscous flows at different Reynolds (Re) number regimes. For relatively slow moving biological/synthetic swimmers of micron size or even smaller, the estimated Re number is typically close to zero (e.g., $\mathrm{Re} \sim 10^{-3}$), and hence the inertia effect is negligible. In this regime, fluid motion is governed by the incompressible Stokes equation, and the fluid-structure interactions (FSIs) can be modeled by using the boundary integral method that integrates the singularity solutions distributed on the particle surface via Green's functions [20]. Truncated multipole expansions are commonly used to facilitate numerical evaluation of the integrals with desired accuracy [21–23]. For rod-like microparticles such as bacteria (e.g., *E. coli*) or biopolymers (e.g., microtubule), a special type of boundary integral method, the so-called slender body theory [24], is preferred to use. In this method, singularity solutions are appropriately distributed along particles' centerline so that the no-slip velocity condition on the rod surface is satisfied for matched asymptotic expansions of solutions. Various different types of slender body models were developed, from the local models [25] that adopt a linear relation between the local centerline velocity and the force per unit length exerting upon the fluid, to the global models [26] that incorporate self-interactions of rods as well as their hydrodynamic interactions with other structures and obstacles. To further facilitate large-scale simulations for many particles that are hydrodynamically interacting, fast summation methods such as the Ewald method [27] and fast multipole method [28] have been implemented to speed up numerical calculation of boundary integrals with the Stokesian kernels (e.g., Stokeslet, Rotlet, Stresslet).

For swimmers of a larger size (e.g., hundreds of microns), the resultant inertial force can be non-negligible compared to the Stokes drag. In fact, some small organisms are able to take advantage of the inertial forces to achieve enhanced free-swimming, escaping, energy saving, as well as mixing in collections [29–33]. At a finite Re, the incompressible Navier-Stokes (N-S) equation is used to describe the fluid motion, and FSIs are typically solved by using the grid-based methods (e.g., finite difference, finite elements). Compared to the sharp-interface methods that employ body-fitted meshes to resolve interfaces or fluid-solid boundaries, Cartesian grid methods that employ non-body-fitted meshes are more convenient in handling moving boundaries or large deformations of particles that have complex geometries. For example, the Immersed Boundary (IB) type methods have been widely used in simulating swimming organisms such as nematode and amoeboid [34, 35]. Moreover, Ardekani *et al.* have developed the distributed Lagrange-multiplier-based finite-volume method to study various aspects of active particles, including wall-effect, pair-interactions, collective behaviors and unsteady inertial effects in both Newtonian and viscoelastic liquids [3, 31, 32, 36, 37].

To explore non-equilibrium physics of active suspensions at different Reynolds number regimes, especially at high concentration where the collective behaviors are prominent due to the enhanced particle-particle interactions, it is desirable to develop accurate and efficient simulation tools that are capable of resolving the long and short range interactions simultaneously for a large number of hydrodynamically-mediated active particles with complex shapes. In this paper, we present a direct-forcing fictitious domain (FD) method to study dynamics of swimming microparticles at small and finite Re numbers. The direct-forcing FD method was originally developed by Yu and Shao [38], and has been successfully used in studying various types of fluid-structure interactions. In particular, it has been used in resolving how neutrally buoyant particles interact with turbulent flows in a horizontal channel, as well as investigating the impact of particle-fluid coupling on the flow instability and turbulence transition in pipe flows and heat transfer [39–41]. Very recently, a parallel strategy has been implemented by Lin *et al.* [42] to investigate particle-laden turbulent duct flows and the effects of particle inertia on the turbulent channel flow [42, 43]. The method presented here is an extension of the direct-forcing FD method in simulating active matter systems

via the classical "Squirmer" model in which microswimmers are treated as rigid spheres with a prescribed surface velocity field [44, 45]. We perform a series of numerical studies to examine the algorithm's performance at both low and finite Reynolds numbers, including the dynamics of a free-swimming Squirmer and two side-by-side Squirmers, statistic properties of quasi-2D collective dynamics, as well as transport behavior of macro obstacles in active suspensions.

The rest of paper is organized as follows: In Section II we briefly describe the details of the mathematical model and the numerical algorithm, including the Squirmer model that mimics the microswimmer motion, the computation scheme of the FD solver, as well as the contact model for collisions between particles and obstacles. In section III, a series of numerical simulations are performed for the "Pusher" and "Puller" particles. We first study the benchmark problems of a single free-swimming particle and their pair interactions when moving side-by-side. Then we investigate the collective dynamics of a monolayer of active particles immersed in a bulk fluid by examining the flow patterns and particle structures at various different concentrations through spatiotemporal correlation functions. The inertia effect on collective dynamics at a finite Re is also examined. Finally, at a low Reynolds number, we study migration of a freely-moving short cylinder (circular and wedge-like) when interacting with a Pusher monolayer, and reveal the physical mechanisms of the observed directional movement that is dominated by cylinder-particle collision resultant from an anisotropic shape. Conclusions are made in Section IV.

II. MATHEMATICAL MODEL AND NUMERICAL METHOD

A. Squirmer model for near-body dynamics

To begin with, we briefly introduce the micromechanical model. A classical Squirmer model is implemented in our algorithm, where the microswimmers are treated as spherical rigid particles [3, 32, 36, 44, 46–48]. In general, two types of motion, i.e., "Pusher" and "Puller", are modeled by prescribing a surface velocity field, depending on whether they gain thrust from rear (e.g., *E. coli*) or front (e.g., *Chlamydomonas*) body movement. In this approach, generation of the near-body fluid motion is projected on an effective spherical "envelope" around the swimmer to represent various different modes of rigid-body motion and deformation [47]. The induced fluid velocity field can be represented as:

$$\mathbf{u} = \mathbf{e} \cdot \left(\frac{\mathbf{rr}}{r^2} - \mathbf{I}\right) \sum_{n \geq 1} \frac{2}{n(n+1)} B_n {P_n}'(\frac{\mathbf{e} \cdot \mathbf{r}}{r}), \tag{1}$$

where $\mathbf{e}$ is the orientation vector of the Squirmer, B_n represents the nth mode of the tangential surface motion [46], P_n and P_n' are the nth *Legendre* polynomial and its derivative, and $\mathbf{r}$ is the position vector and $r = |\mathbf{r}|$. Following previous studies [3, 32, 36, 48], we adopt a reduced model with two "squirming modes" that describe a steady tangential surface velocity field in the body frame:

$$u_\theta^s(\theta) = B_1 \sin\theta + B_2 \sin\theta \cos\theta, \tag{2}$$

where $\theta = \arccos(\mathbf{e} \cdot \mathbf{r}/r)$ is the polar angle between the position vector $\mathbf{r}$ and the swimming direction $\mathbf{e}$, and B_1 and B_2 are the coefficients for the two squirming modes. While simple, Eq. (2) is adequate to distinguish the basic swimming types of microorganisms by choosing the sign of the parameter $\beta = B_2/B_1$. The Pusher (Puller) particles corresponds to situations when β is negative (positive); while the neutral particles with a symmetric surface velocity distribution is defined when $\beta = 0$. In the Stokes flow regime, the steady-state swimming speed U_0 of a Squirmer in free space

can be analytically calculated as $U_0 = 2B_1/3$ [3, 44, 49]. Since in our FD method body forces are distributed in the entire interior region of particle, we impose a solenoidal *volumetric* velocity field $\mathbf{u}_a$ which was used by Li *et al.* [3, 36]

$$\mathbf{u}_a = \left[\left(\frac{r}{a}\right)^m - \left(\frac{r}{a}\right)^{m+1}\right]\left(u_\theta^s \cot\theta + \frac{du_\theta^s}{d\theta}\right)\mathbf{e}_r + \left[(m+3)\left(\frac{r}{a}\right)^{m+1} - (m+2)\left(\frac{r}{a}\right)^m\right] u_\theta^s \mathbf{e}_\theta, \quad (3)$$

where a is the radius of the spherical Squirmer, $\mathbf{e}_r$ and $\mathbf{e}_\theta$ are the unit vectors along the $r-$ and $\theta-$direction, and m is an arbitrary positive integer. In our simulation, as shown in the schematic in Fig. 1(a), collocation points are distributed uniformly on layers of concentric spherical surfaces in the entire particle domain [38].

In addition to hydrodynamic interactions, we implement a soft-sphere collision model to resolve the short-ranged collisions. It calculates a repulsive force between the ith and jth objects (e.g., particles, rigid obstacles and walls) that are close to contact as: [42, 50]:

$$\mathbf{f}_{ij} = \kappa_0 \left(1 - \frac{d}{d_c}\right)\mathbf{n} \quad (4)$$

where the constant κ_0 is typically chosen as $10^3 \sim 10^4$ of particle mass, d is the particle inter-distance, d_c is a cut-off distance to define the "contact" zone which is dependent on mesh size Δx (typically $d_c = \Delta x \sim 2\Delta x$), and $\mathbf{n}$ is a unit vector pointing in the direction where contact occurs. It has to be mentioned that here we consider non-Brownian particle motions by assuming that swimming micro-organisms are in the high Peclet limit where the advective forces produced by particle activity dominate over random thermal forces.

B. Direct-forcing fictitious domain method

The micromechanical model of non-Brownian active particles is implemented in the FD method [38, 39, 43] whose computation scheme is discussed in this section. In general, the FD method fills the interior domain of rigid particles with fluid, and distribute a pseudo body-force field over the particle inner domain to enforce the interior "fictitious" fluid movement to follow the rigid body motion. The FD method was originally developed by Glowinski *et al.* [50, 51]. It employs a distribution of body force (or Lagrange multipliers) in the solid domain via a weak formulation, and enforce the fluid-particle coupling through fluid/solid phase iterations. Alternatively, our method computes the body forces on the Lagrangian meshes from the no-slip boundary conditions explicitly, the same as that used in the direct-forcing IB methods [52, 53]. The physical variables are mapped between the two overlaid meshes through a discrete δ-function. One merit of our method is that no inner-iterations are needed to achieve convergence when solving the fluid-solid coupling, which, together with efficient parallelization, significantly improves computation efficiency.

In the following, we use $P(t)$ and $\partial P(t)$ represent the solid particle domain and its boundary, Ω_f the real fluid region, and Ω the entire domain comprising both interior and exterior of the body. The momentum equation for the fluid flow is governed by the incompressible Navier-Stokes equation throughout the entire computational domain:

$$\rho_f \frac{D\mathbf{u}}{Dt} = \nabla \cdot \boldsymbol{\sigma}, \qquad \text{in } \Omega_f \quad (5)$$

where $D/Dt = \partial\mathbf{u}/\partial t + \mathbf{u}\cdot\nabla\mathbf{u}$ is a material derivative, ρ_f is the fluid density, $\mathbf{u}$ the fluid velocity, $\boldsymbol{\sigma}$ is the fluid stress.

The rigid-particle motion is governed by the Newton's law:

$$M\frac{d\mathbf{U}_p}{dt}=\left(1-\frac{1}{\rho_r}\right)M\mathbf{g}+\mathbf{F}_H,\quad \frac{d\left(\mathbf{J}\cdot\boldsymbol{\omega}_p\right)}{dt}=\mathbf{T}_H, \tag{6}$$

where d/dt is a Lagrangian time derivative, ρ_r is the solid-fluid density ratio defined by $\rho_r=\rho_s/\rho_f$, $\mathbf{g}$ is the gravitational acceleration. Here M, $\mathbf{J}$, $\mathbf{U}_p$ and $\boldsymbol{\omega}_p$ respectively correspond to the particle mass, moment of inertia tensor, translational velocity and angular velocity. In the above $\mathbf{F}_H$ and $\mathbf{T}_H$ are the hydrodynamic force and torque on the particle, respectively, which are defined as

$$\mathbf{F}_H=\int_{\partial P}\mathbf{n}\cdot\boldsymbol{\sigma}dS,\qquad \mathbf{T}_H=\int_{\partial P}\mathbf{r}\times\left(\mathbf{n}\cdot\boldsymbol{\sigma}\right)dS \tag{7}$$

where $\mathbf{n}$ is the unit outward normal vector on the solid particle surface ∂P. As mentioned before, the interior fictitious fluid motion is governed by the momentum-balance relation:

$$\rho_f\frac{D\mathbf{u}}{Dt}=\nabla\cdot\boldsymbol{\sigma}+\boldsymbol{\lambda},\qquad \text{in } P\left(t\right) \tag{8}$$

and is constrained by the rigid body motion:

$$\mathbf{u}=\mathbf{U}_p+\boldsymbol{\omega}_p\times\mathbf{r}+\mathbf{u}_a \tag{9}$$

where $\boldsymbol{\lambda}$ is the pseudo body-force defined in the solid particle domain (Lagrange-multiplier). Integrating equations (8) and $\mathbf{r}\times$ (8) over the solid particle interior and substituting into equations (7) yield:

$$\mathbf{F}_H=\frac{M}{\rho_r}\frac{d\mathbf{U}_p}{dt}+\int_P\rho_f\frac{d\mathbf{u}_a}{dt}d\mathbf{x}-\int_P\boldsymbol{\lambda}d\mathbf{x}, \tag{10}$$

$$\mathbf{T}_H=\frac{1}{\rho_r}\frac{d\left(\mathbf{J}\cdot\boldsymbol{\omega}_p\right)}{dt}+\int_P\rho_f\left(\mathbf{r}\times\frac{d\mathbf{u}_a}{dt}\right)d\mathbf{x}-\int_P\mathbf{r}\times\boldsymbol{\lambda}d\mathbf{x}. \tag{11}$$

Taking into account the fact that the imposed active velocity does not generate net force and torque (i.e., $\int_P\mathbf{u}_a d\mathbf{x}=0$, $\int_P\mathbf{r}\times\mathbf{u}_a d\mathbf{x}=0$) and substituting Eqs. (10) and (11) into (6), we eventually derive:

$$\left(1-\frac{1}{\rho_r}\right)M\left(\frac{d\mathbf{U}_p}{dt}-\mathbf{g}\right)=-\int_P\boldsymbol{\lambda}d\mathbf{x},\quad \left(1-\frac{1}{\rho_r}\right)\frac{d\left(\mathbf{J}\cdot\boldsymbol{\omega}_p\right)}{dt}=-\int_P\mathbf{r}\times\boldsymbol{\lambda}d\mathbf{x}. \tag{12}$$

The governing equations can be non-dimensionalized by introducing the following scales: $L_c=a$ for length, $U_c=U_p$ (i.e., particle moving speed) for the velocity, L_c/U_c for time, $\rho_f U_c^2$ for the pressure, $\rho_f U_c^2/L_c$ for the pseudo body-force. The dimensionless governing equations for the incompressible fluid and particle are summarized as follows (Note that we use the same notation for the dimensionless variables as the dimensional ones):

$$\frac{\partial\mathbf{u}}{\partial t}+\mathbf{u}\cdot\nabla\mathbf{u}=\frac{1}{\mathrm{Re}}\nabla^2\mathbf{u}-\nabla p+\boldsymbol{\lambda},\ \ \nabla\cdot\mathbf{u}=0\quad \text{in } \Omega \tag{13}$$

$$\mathbf{u}=\mathbf{U}_p+\boldsymbol{\omega}_p\times\mathbf{r}+\mathbf{u}_a,\quad \text{in } P(t) \tag{14}$$

$$\left(\rho_r-1\right)V_p^*\left(\frac{d\mathbf{U}_p}{dt}-Fr\frac{\mathbf{g}}{g}\right)=-\int_P\boldsymbol{\lambda}d\mathrm{x},\quad \left(\rho_r-1\right)\frac{d\left(\mathbf{J}^*\cdot\boldsymbol{\omega}_p\right)}{dt}=-\int_P\mathbf{r}\times\boldsymbol{\lambda}d\mathrm{x}. \tag{15}$$

In the above equations, p represents the fluid pressure, the Reynolds number defined by $\mathrm{Re}=\rho_f U_c L_c/\mu$ the fluid viscosity, the Froude number defined by $Fr=gL_c/U_c^2$, the dimensionless particle volume defined by $V_p^*=U_c/L_c^3$, and the dimensionless moment of inertia tensor defined by $\mathbf{J}^*=\mathbf{J}/\rho_s L_c^5$. In all the cases studied here, we only consider micro-swimmers to be neutrally-buoyant particles with ρ_r=1.0, and hence neglect the gravitational force by choosing $Fr=0$.

C. Computational scheme

A fractional-step time scheme is used to decouple the combined system (13)-(15) into two sub-problems.

(1)Fluid sub-problem for $\mathbf{u}^*$ and p^{n+1} :

$$\frac{\mathbf{u}^*-\mathbf{u}^n}{\Delta t}-\frac{1}{2\mathrm{Re}}\nabla^2\mathbf{u}^*=-\nabla p^{n+1}-\frac{1}{2}\left[3(\mathbf{u}\cdot\nabla\mathbf{u})^n-(\mathbf{u}\cdot\nabla\mathbf{u})^{n-1}\right]+\frac{1}{2\mathrm{Re}}\nabla^2\mathbf{u}^n+\boldsymbol{\lambda}^n, \tag{16}$$

$$\nabla\cdot\mathbf{u}^*=0. \tag{17}$$

We employ a standard fractional step procedure to solve the above N-S equation system in fixed Eulerian domain with a uniform grid size Δx. Eqs. (16) and (17) are decomposed into three steps:

(a) Helmholtz velocity equation:

$$\frac{\mathbf{u}^\#-\mathbf{u}^n}{\Delta t}-\frac{\nabla^2\mathbf{u}^\#}{2\mathrm{Re}}=-\nabla p^n-\frac{1}{2}\left[3(\mathbf{u}\cdot\nabla\mathbf{u})^n-(\mathbf{u}\cdot\nabla\mathbf{u})^{n-1}\right]+\frac{\nabla^2\mathbf{u}^n}{2\mathrm{Re}}+\boldsymbol{\lambda}^n. \tag{18}$$

(b)Poisson pressure equation:

$$\nabla^2\phi=\frac{\nabla\cdot\mathbf{u}^\#}{\Delta t}, \tag{19}$$

(c)Correction of velocity and pressure:

$$\mathbf{u}^*=\mathbf{u}^\#-\Delta t\nabla\phi,\quad p^{n+1}=p^n+\phi. \tag{20}$$

A second-order half-staggered finite difference scheme is used for spatial discretization. And the multi-grid iterative method is performed to solve Eqs. (18) and (19).

(2) Particle sub-problem for $\mathbf{U}_p^{n+1}$, $\boldsymbol{\omega}_p^{n+1}$, $\boldsymbol{\lambda}^{\boldsymbol{n+1}}$, $\mathbf{u}^{n+1}$:

$$\frac{\mathbf{u}^{n+1}-\mathbf{u}^*}{\Delta t}=\boldsymbol{\lambda}^{n+1}-\boldsymbol{\lambda}^n \tag{21}$$

$$\mathbf{u}^{n+1}=\mathbf{U}_p^{n+1}+\boldsymbol{\omega}_p^{n+1}\times\mathbf{r}+\mathbf{u}_a \tag{22}$$

$$(\rho_r-1)\,V_p^*\left(\frac{\mathbf{U}_p^{n+1}-\mathbf{U}_p^n}{\Delta t}-Fr\frac{\mathbf{g}}{g}\right)=-\int_p\boldsymbol{\lambda}^{n+1}d\mathbf{x} \tag{23}$$

$$(\rho_r-1)\left[\frac{\mathbf{J}^*\cdot\left(\boldsymbol{\omega}_p^{n+1}-\boldsymbol{\omega}_p^n\right)}{\Delta t}+\boldsymbol{\omega}_p^n\times\left(\mathbf{J}^*\cdot\boldsymbol{\omega}_p^n\right)\right]=-\int_p\mathbf{r}\times\boldsymbol{\lambda}^{n+1}d\mathbf{x} \tag{24}$$

Substituting (21),(22) into (23),(24) yields

$$\rho_r{V_p}^*\frac{\mathbf{U}_p^{n+1}}{\Delta t}=(\rho_r-1)V_p^*(\frac{\mathbf{U}_p^n}{\Delta t}+Fr\frac{\mathbf{g}}{g})+\int_P\left(\frac{\mathbf{u}^*-\mathbf{u}_a}{\Delta t}-\boldsymbol{\lambda}^n\right)d\mathbf{x}, \tag{25}$$

$$\rho_r\frac{\mathbf{J}^*\cdot\boldsymbol{\omega}_p^{n+1}}{\Delta t}=(\rho_r-1)[\frac{\mathbf{J}^*\cdot\boldsymbol{\omega}_p^n}{\Delta t}-\boldsymbol{\omega}_p^n\times(\mathbf{J}^*\cdot\boldsymbol{\omega}_p^n)]+\int_P\mathbf{r}\times\left(\frac{\mathbf{u}^*-\mathbf{u}_a}{\Delta t}-\boldsymbol{\lambda}^n\right)d\mathbf{x}. \tag{26}$$

In the above equations (25)-(26), all the right-hand side terms are known quantities, so $\mathbf{U}_p^{n+1}$ and $\boldsymbol{\omega}_p^{n+1}$ are obtained directly. Then $\boldsymbol{\lambda}^{n+1}$ that are defined at the Lagrangian nodes can be determined by:

$$\boldsymbol{\lambda}^{n+1} = \frac{\mathbf{U}_p^{n+1} + \boldsymbol{\omega}_p^{n+1} \times \mathbf{r} + \mathbf{u}_a - \mathbf{u}^*}{\Delta t} + \boldsymbol{\lambda}^n. \tag{27}$$

Finally, the fluid velocity $\mathbf{u}^{n+1}$ at the Eulerian nodes are determined as follow:

$$\mathbf{u}^{n+1} = \mathbf{u}^* + \Delta t(\boldsymbol{\lambda}^{n+1} - \boldsymbol{\lambda}^n). \tag{28}$$

We use a tri-linear function to serve as the discrete delta function that maps quantities between the Lagrangian and Eulerian nodes in the equations (25)-(28). It has been shown that with the explicit direct-forcing scheme for solving the particle sub-problem, we are able to avoid the singularity at $\rho_r = 1$ [38]. Then particle position can be determined from the kinematic equation:

$$\frac{d\mathbf{X}}{dt} = \mathbf{U}_p. \tag{29}$$

Additionally, it is important to mention a few useful numerical techniques in dealing with the coupling of Eulerian and Lagrangian meshes. First of all, distribution of the Lagrangian collocation points on the spherical particle has to be approximately homogeneous, and the average distance between them needs to be close to the background Eulerian grid size. Secondly, retraction of Lagrangian points from the particle surface need to be tuned in order to reduce system stiffness, in order to eliminate numerical oscillations caused by interpolations between the two overlaid meshes [38]. While the optimal distance is case-dependent, we find for a finite Re the typical retraction length is approximately $\Delta x/5 \sim \Delta x/3$. Thirdly, we need to use a small time step (e.g., one tenth of the time step of the N-S solver) for the collision model due to the fact that the repulsive forces between approaching particles are computed explicitly. An efficient parallel algorithm based on Message Passing Interface (MPI) has been implemented to speed up computation. The reader is referred to the previous work by Lin *et al.* [43] for more details about parallelization.

III. NUMERICAL RESULTS

A. Benchmark problems: single particle dynamics and pair interactions

We first examine the migration velocity of a single free-swimming Squirmer ($a = 1.0$) in an infinite domain at $\mathrm{Re} = 0.01, 1.0$, for Pusher ($\beta < 0$), Puller ($\beta > 0$), and neutral ($\beta = 0$) particle. Here we impose a far-field condition in its swimming (z) direction (i.e., $\frac{\partial \mathbf{u}}{\partial z} = \mathbf{0}$), and assume periodicity in both the x and y directions. Starting from a zero initial velocity, all three types of Squirmer particles eventually approach steady state with a constant moving speed $U_p = |\mathbf{U}_p|$ shown in Fig. 1(a). The velocities are normalized by the steady moving speed of the neutral particle which is independent of the Reynolds number. At the two Re numbers, we find excellent agreements with the previous numerical studies [3, 54] and analytical predictions [32, 49]. As shown in panels(b-d) of Fig. 1 for the in-plane fluid velocity fields plotted in the co-moving coordinates with the motile particle, the induced flow field is axisymmetric with a pair of vortex rings attached in front of (behind) the Pusher (Puller) particle, and approximately symmetric for the neutral particle.

Robustness of our simulation results has been examined in convergence tests. In general, we find accurate results can be obtained when choosing the square computational domain size 15 times bigger than the particle diameter, time step Δt less than 0.002, the Eulerian grid size $\Delta x (= \Delta y = \Delta z)$ smaller than $a/8$, and the ratio of the two sets of mesh (Lagrangian/Eulerian) between 1.0 and

TABLE I: Benchmark problem for single particle dynamics ($\mathrm{Re} = 1.0; \beta = -3, 0, 3$)

	Domain size	Number of grid points	Time step
Mesh1	$32 \times 32 \times 32$	$256 \times 256 \times 256$	0.002
Mesh2	$32 \times 32 \times 32$	$512 \times 512 \times 512$	0.001

TABLE II: Benchmark problem for pair interactions ($\mathrm{Re} = 0.1, \beta = -5, 5, \delta\mathrm{y} = 1.0, \delta\mathrm{z} = 10.0$)

Domain size	Number of grid points	Time step
$32 \times 32 \times 32$	$256 \times 256 \times 256$	0.002

1.2. Depending on the size of the problem, we use 256 - 512 grid points in each spatial direction to resolve the background Eulerian mesh, and perform parallel computations on 64 - 128 Intel cores. We have summarized the relevant computation parameters in Table I and II.

Next we examine the pair interactions between two side-by-side Squirmers ($a = 1.0$) that are initially co-located in the $y - z$ plane, and move in the $z-$direction. Figure 2(a) shows the trajectories of the two Squirmers moving towards each other with the initial separation distance $\delta y = 1.0$ at $\mathrm{Re} = 0.1$. For two Pullers ($\beta = 5$), it is seen that as the two particles move very close, they contact and move away from each other. The calculated particle trajectories agree well with those obtained by Ishikawa *et al.* [55]. For Pushers ($\beta = -5$), an unstable "trapping" state (dotted lines) is observed, during which the two particles stay close to contact for a long time after contact, and may eventually separate along arbitrary directions, which also agrees with the results reported by Li and Ardekani [36].

We then take a close look at the cases where two Squirmers move side-by-side. In panel(b) of Fig. 2, the two Pushers ($\beta = -3$, $\delta y = 2.5$) are seen to first attract to each other, due do the hydrodynamic interactions of the resultant near-body extensile flows. Then they contact and glide for a while until they move away. Similar attractive interactions have been observed when the Pusher particle is swimming close to a rigid wall [3]. The particle trajectories are qualitatively similar before separation, although it is noticed that they experience a longer gliding motion at a small Re. In the inset of (b), we show that a series of results at $\mathrm{Re} = 0.01$ by gradually increasing δy gradually to inhibit the pair interactions, and find the two particles eventually move in straight lines when δ is large, e.g., $\delta y = 8.0$.

On the other hand, the pair interaction of Pullers shown in panel(c) of Fig. 2 is somewhat complicated. When inertia is negligible at a low Re, the two side-by-side Pullers are immediately pushed away from each other, due to the hydrodynamic interactions of the near-body contracting flows, and then approximately move straight together. At finite Re numbers, however, after the initial separation, the two particles are able to make turns and come close again. By slightly shifting their positions (not reported here), we also find the two Puller particles approximately move in the same direction and keep interacting with each other, which agree with the observations in Ref. [55]. In the inset of panel(c), we show that at $\mathrm{Re} = 1.0$ the hydrodynamic interactions indeed generate net pulling forces (i.e., $y-$component of the hydrodynamic force $\mathbf{F}_H$ in Eq. (10)) between the co-moving Pullers.

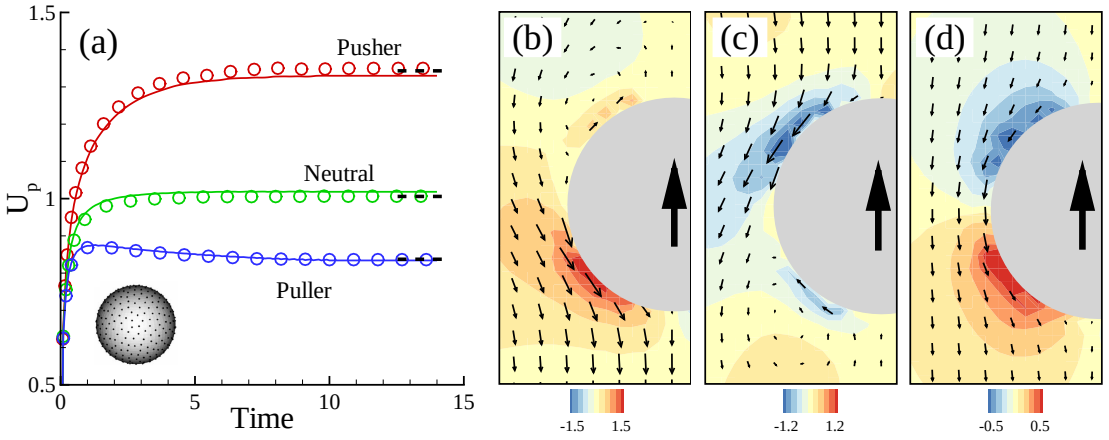

FIG. 1: Free-swimming motion of a single Squirmer particle at Re = 1.0. (a) Translational velocity U_p as a function of time for Pusher ($\beta = -3$), Puller ($\beta = 3$), and neutral ($\beta = 0$) particle, respectively. Solid lines and open circles represent the simulation results obtained by choosing the Eulerian grid size and time step as ($\Delta x = \frac{a}{8}, \Delta t = 0.002$) and ($\Delta x = \frac{a}{16}, \Delta t = 0.001$), respectively. The black dashed lines represent the analytical predictions [49]. Inset: Lagrangian collocation points distribution. Panels(b,c,d) show the in-plane velocity field for (b) Pusher, (c) Puller and (d) neutral particles superimposed on the u velocity component (colorfield) when choosing ($\Delta x = \frac{a}{8}, \Delta t = 0.002$).

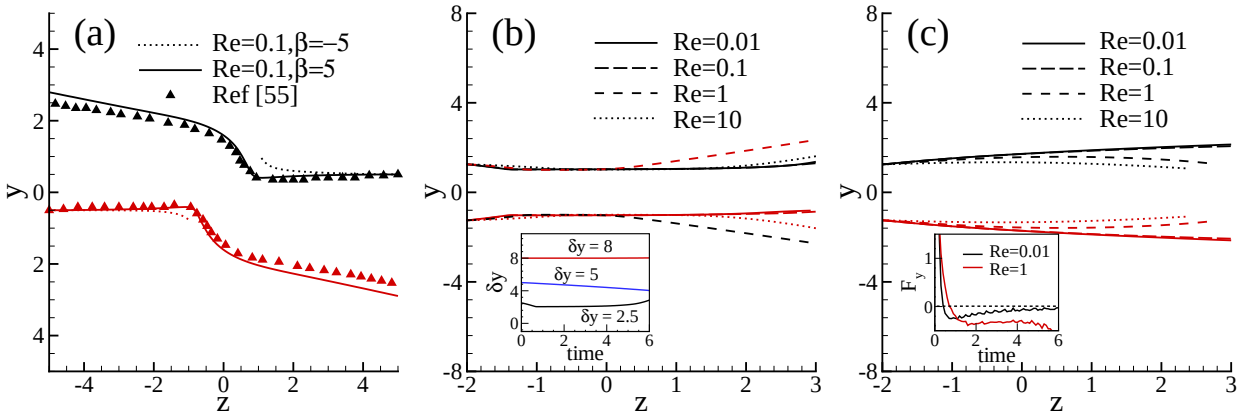

FIG. 2: (a) Comparison of the trajectories of two colliding Squirmer particles ($\beta = \pm 5, a = 1.0$). (b) Trajectories of two side-by-side Pushers ($\beta = -3, a = 1.0$) at various Re numbers. Inset: variation of the separation distance between the two particles as a function of time by changing δy. (c) Trajectories of two side-by-side Pullers ($\beta = 3, a = 1.0$) at various Re numbers. Inset: net force exerted on the Puller particle in the y direction as a function of time.

B. Collective dynamics

In this section, we study quasi-2D collective dynamics of N Pusher and Puller particles ($\beta = \pm 3$, $a = 1.0$) that are confined in a monolayer [56, 57]. We carefully examine the spatio-temporal coherent structures and their statistic properties. In the meantime, we characterize the inertia effect by comparing the computation results at small and finite Re. The simulations are performed over long time periods at various (area) concentrations in a periodic cubic domain of size $L_x = L_y = L_z$. The squirmers' swimming motions (i.e., translation and rotation) are confined at the central plane

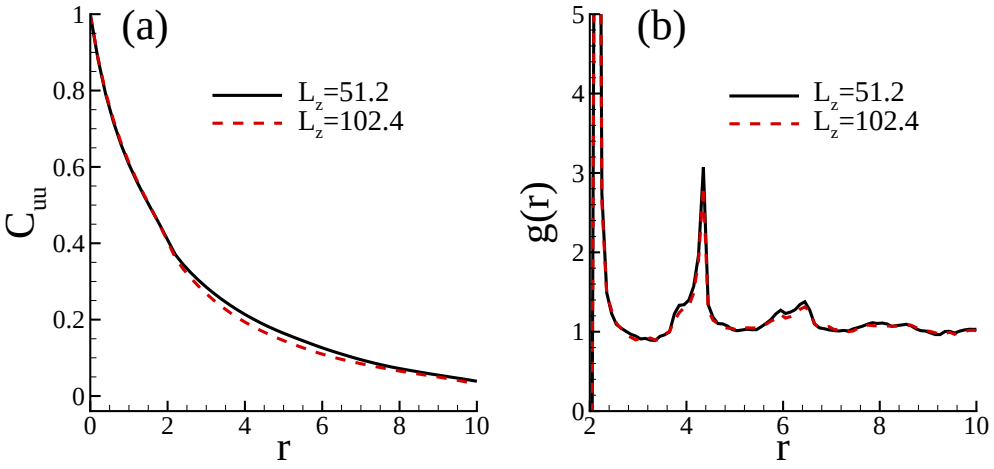

FIG. 3: The normalized velocity-velocity correlation function C_{uu} (a) and pair-distribution function $g(r)$ (b) computed when using two different domain sizes with $L_z = 51.2, 102.4$ at Re $= 0.01$ for a concentrated Puller suspension when choosing $\beta = 3, a = 1.0, \phi = 24\%$.

immersed in a 3D bulk flow, with their initial center-of-mass (C.O.M.) positions and orientations distributed on the $x - y$ plane.

As suggested by Ishikawa and Pedley [56] who chose a domain size much longer in the third dimension ($z-$direction, i.e., $L_z = 10L_x$) to guarantee the mobility matrix to be positive definite in their Stokesian dynamics simulations, we perform convergence tests by comparing statistic measurements (see further discussions below) at Re $= 0.01$ obtained on the two computation domain: (i) $L_x = L_y = L_z = 51.2$ and (ii) $L_x = L_y = 51.2, L_z = 102.4$. As shown in Fig 3 and thereafter, we examine the normalized velocity-velocity correlation function of the fluid flow $\overline{\mathbf{u}(\mathbf{x}, t)}$ (panel (a)),

$$C_{uu}(r) = \frac{< \overline{\mathbf{u}(\mathbf{x}+\mathbf{r}, t) \cdot \mathbf{u}(\mathbf{x}, t)} >}{< \overline{|\mathbf{u}(\mathbf{x}, t)|^2} >}, \tag{30}$$

where the angle bracket <> denotes time average and the overbars denote spatial average, as well as the pair-distribution function $g(r)$ (panel (b)),

$$g(r) = \frac{L_x L_y}{N(N-1)S(r)} \sum_{m=1}^{N} \sum_{n=1, n\neq m}^{N} \delta(r_{mn} - r) \tag{31}$$

where r_{mn} is the distance between squirmers m and n, N is the total number of the squirmers, $S(r)$ is the area of ring of radius r and thickness Δr [3]. The function $\delta(r_{mn} - r)$ is defined as 1 when $|r_{mn} - r| < \Delta r/2$, and 0 otherwise. Note that mathematically, $\rho_0 g(r) 2\pi r dr$, where $\rho_0 = N/L^2$ is the bulk number density of particles, is the average number of particles whose distance from a central particle is between $r - \triangle r/2$ and $r + \triangle r/2$ [58]. Excellent agreements between the simulation results suggest that the domain size is sufficiently large to minimize the boundary effect.

In Fig. 4, we show the in-plane (i.e., u and v component) velocity vector field of Pusher suspensions at three different concentrations at Re $= 0.01$. As a typical case of low concentration ($\phi = 6\%$, $N = 50$) shown in panel(a) of Fig. 4, the induced fluid is seemingly weak and only significant in the particle vicinity owing to their fast decay. More correlated structures are observed at a finite concentration as shown in panel(b) when $\phi = 24\%$ ($N = 200$). Further increasing particle

concentration (e.g., $\phi = 48\%$, $N = 400$, panel(c)) nevertheless leads to small and seemingly disconnected flow structures, which is likely due to the enhanced steric interactions between particles with more frequent collisions.

Likewise, we show the flow fields of Puller suspensions in panels(e-f) of Fig. 4 for the same three concentrations. Compared to Pusher particles, one significant difference is that while interacting hydrodynamically, Puller particles tend to move together to form clusters [56], which effectively facilitates separation of the fluid and the particle phases. Especially at a high concentration as shown in panel(f), near-body interactions lead to a 2D hexagonal lattice, similar to the active crystalline structures observed for colloidal surfers [59]. For both Pusher and Puller suspensions, we quantify the local sixfold structure by calculating the so-called bond parameter, $|q_6^{(k)}|^2 \in [0, 1]$, in order to measure of the orientational order of particle k, where $q_6^{(k)} = \frac{1}{6}\sum_{j\in N_6^{(k)}} \exp(i6\alpha_{kj})$ [60]. The sum goes over the six nearest neighboring particle k; while the parameter α_{kj} represents the angle between the relative position $\mathbf{r}^k - \mathbf{r}^j$ and a randomly selected axis. Not surprisingly, for the Pushers in panels(a-c), $|q_6|^2$ is low ($|q_6|^2$ less than 0.4) at all concentrations, which reflects the local disorder due to mixing. In panels(e-g), $|q_6|^2$ effectively captures the concentration-dependent hexagonal lattice formation, with the highest value ($|q_6|^2 \sim 0.9$) occurring within the particle granules where microparticles are tightly packed.

As the result of fluid-solid phase separation at high concentrations (e.g., panels(f) and (g)), the in-plane velocity field exhibit source-like structures as the flow moves from bulk towards the moving boundaries of particle granules, suggesting that the surface flow is highly compressible. In panels(d) and (h), more complex 3D flow structures can be visualized through the (u, w) velocity field projected on the $x - z$ plane extracted at $y = 25.6$ (marked by the black dashed lines in panels(c) and (g)). Apparently, the induced flows are seen to be much stronger for the Puller case with slow decays in the $z-$direction (see inset in panel(h)).

In Fig. 5, the above 2D velocity fields are characterized via probability density functions (PDFs) for fluctuations of the $u-$ velocity component $u' = u- < \overline{u} >$, which can be normalized by multiplying the root mean square value $\sigma' = \sqrt{< \overline{u'^2} >}$, i.e., $\sigma' \times PDF$. Here the angle bracket and the overbar denote a time and a spatial average, respectively. (Note that here we only use the data outside of the spherical shapes and have ignored the internal fictitious fluid motions.) For both Pushers and Pullers, the standard deviations are seen to be nearly symmetric and independent of the Reynolds number. For the dilute cases, their disturbance deviations appear to be significantly different from a standard Gaussian distribution, with sharper peaks around zero. As the concentration increases, the PDFs exhibit wider and wider spectrum due to the enhanced active flows. For the dense cases at $\phi = 48\%$ for both Puller and Pusher cases, the PDFs approximately fit a Gaussian curve, somewhat reminiscent of the chaotic flows induced by active rod suspensions [61].

To obtain more quantitative understandings of the collective dynamics, as well as the inertia effects on the pattern formation and particle structures, we further examine the spatial and temporal correlation functions that are measured at late time as the system reaches quasi-steady state. Figure 6 exhibits the measured C_{uu} in (30) for the in-plane flows at different concentrations which, again, suggest enhanced collective behaviors for dense Pusher and Puller suspensions, especially at a low Reynolds number. As suggested by the velocity vector fields in Fig. 4, apparently the flow structures are more correlated for Puller suspensions. Particle "crystallization" and the resultant phase separation is reflected by a slow decay of C_{uu} in panel(a) of Fig. 6 at $\phi = 24\%, 48\%$ and $\mathrm{Re} = 0.01$, leading to a much longer correlation length. Interestingly, the negative values of C_{uu} (or anti-correlation) at $\phi = 48\%$ suggests that oppositely directed flow patterns appear when r is larger than certain cut-off length r_c (in this case $r_c \approx 15$). It is largely due to the emergent source-like bulk flows set within the particle granules. The cut-off length r_c somewhat characterizes the length scale of the mean spatio-temporal patterns, as suggested by Fig. 4(g) where the

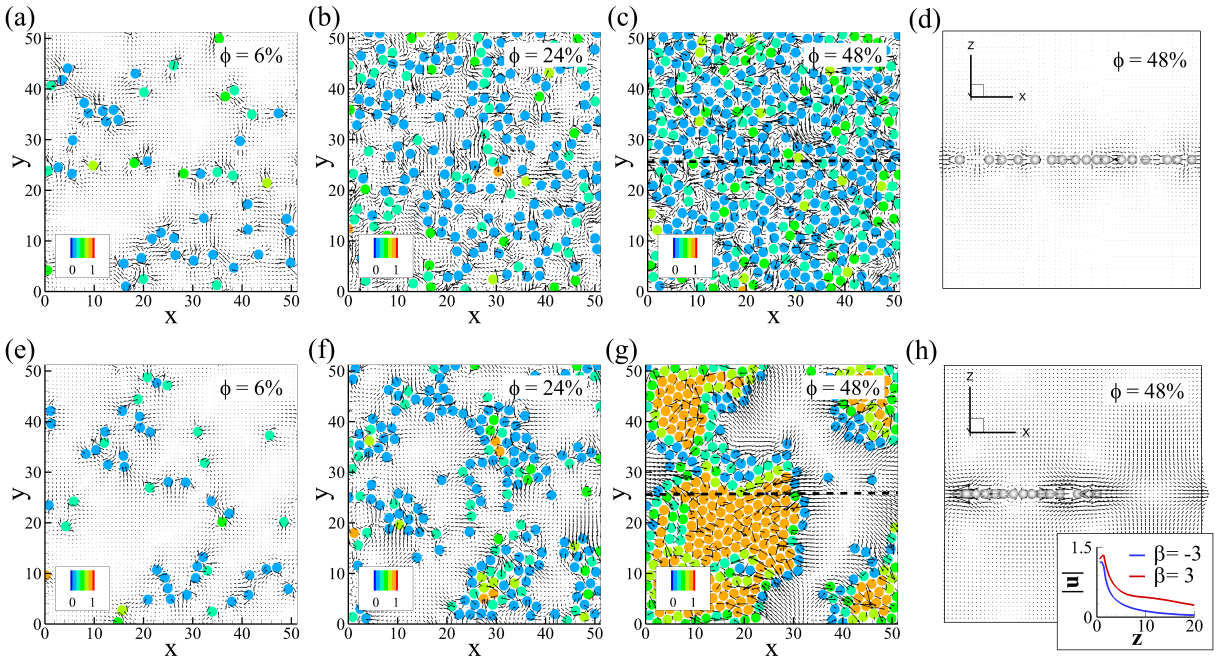

FIG. 4: Velocity vector fields for a monolayer of Pushers ($\beta = -3$, top row) and Pullers ($\beta = 3$, bottom row) at three concentrations (area fraction) at Re $= 0.01$. Panels(d,h): In-plane velocity fields on the (x, z) plane extracted at $y = 25.6$ (marked by the dashed line in panel(c) and (g)) at $\phi = 48\%$ to reveal the 3D flow structures. Inset in (h): Comparison of velocity decay in the $z-$directionl for the Pusher and Puller cases. For panels(a-c) and (e-g), the particle color shows the bond parameter $|q_6^{(k)}|^2 \in [0, 1]$ [60].

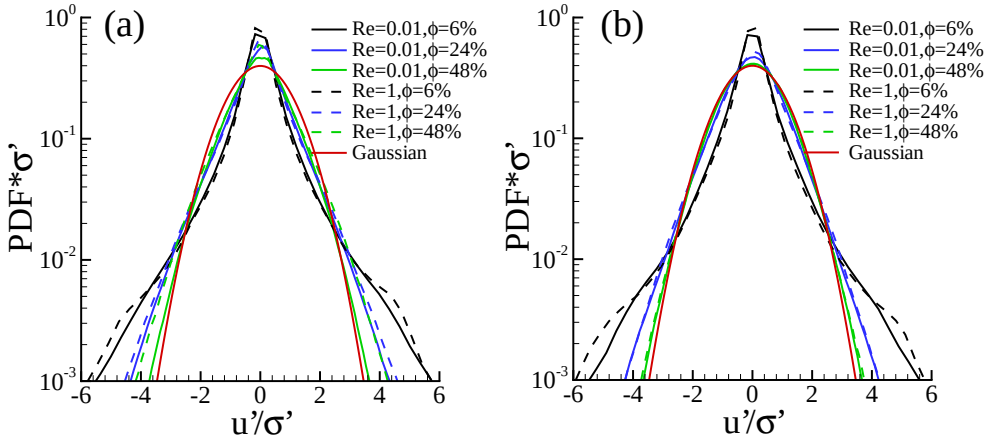

FIG. 5: Normalized Probability density function $PDF \times \sigma'$ as a function of in-plane fluctuation quantity u'/σ' at the different concentrations and Re $= 0.01, 1.0$: (a)Puller ($\beta = 3$), (b)Pusher ($\beta = -3$).

flow velocities are approximately in the opposite direction along the two sides of the fluid-solid boundaries. As Re increases, the induced flows appear to more uncorrelated for both Pusher and Puller cases. Especially for the Pusher suspensions shown in panel(b), the values of C_{uu} sharply drops to zero in all cases, and even collapse onto a certain universal curve at Re $= 1$ independent of concentration.

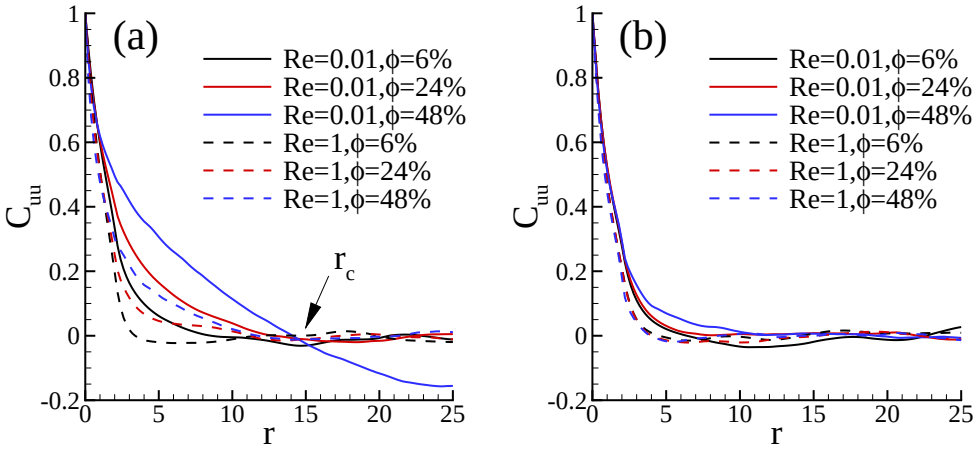

FIG. 6: Normalized velocity-velocity correlation function C_{uu} at the different concentrations and Re $= 0.01, 1.0$: (a)Puller ($\beta = 3$), (b)Pusher ($\beta = -3$).

After analyzing the induced flows, we then present the spatial correlation function of particle velocity $\mathbf{U}_p$ in Fig. 7, which is defined by

$$I_p(r) = \frac{\left\langle \overline{\mathbf{U}_p(\mathbf{x},t) \cdot \mathbf{U}_p(\mathbf{x}+\mathbf{r},t)} \right\rangle}{\left\langle |\overline{\mathbf{U}_p(\mathbf{x},t)}|^2 \right\rangle} \tag{32}$$

where $r = |\mathbf{r}| \geq 2$ represents the relative distance between two particles. The angle bracket <> represents a time average while the overbar denotes an average taken for all particles. Here we only consider suspensions with a finite or high concentration (i.e., $\phi = 12\%, 24\%, 48\%$) where non-trivial particle structures are formed. For the less-concentrated cases at $\phi = 12\%$ ($N = 100$) in panels(a) and (b), I_p is maximum at $r = 2$ (i.e., swimmer diameter) due to pair-interaction, and then quickly drops to zero. Particle velocities are strongly correlated for the dense Puller cases (e.g., $\phi = 48\%$) in panel(a) with multiple peaks, which suggests that neighboring swimmers tend to move collectively in an approximately similar direction. The corresponding particle topological structures are characterized by the pair-distribution function in (31) in Fig. 8. For most cases for different swimmers and Reynolds numbers, $g(r)$ shows an initial peak at $r = 2$ and then quickly decays to zero, suggesting a near-body cluster formation which has been observed in both Brownian and non-Brownian active particle systems [3, 62]. Especially, Pusher particles are seen to easily become uncorrelated when r goes beyond 2. On the other hand, for dense Puller suspensions, their hexagonal lattice is reflected by the main peak at $r = 2$, following by a series of double-peak structures at $r = 4, 6, 8, ...$ [3, 58, 62].

Furthermore, we measure the PDFs of the particle speed magnitude $|\mathbf{U}_p|$, as shown in Fig. 9. Generally speaking, its distribution approximately centers around the single-swimmer velocity computed in section III A. For both Pushers and Pullers, we observe that increasing the particle concentration leads to wider velocity spectrums as particle swim collectively. Different from the induced flows, the PDFs of the Pushers and Pullers are seen to be very similar at Re $= 0.01$ for all concentrations. According to the theoretical predictions at a finite Reynolds number by Li and Ardekani [3, 36], the single particle moving speed is approximately $U_p \approx 1 - 0.15\beta$Re. Therefore, at least for a dilute suspension, the inertia effect tends to shift the single-swimmer speed towards left (i.e., close to zero) for Pullers and towards right (i.e., larger velocity) for Pushers, with narrower

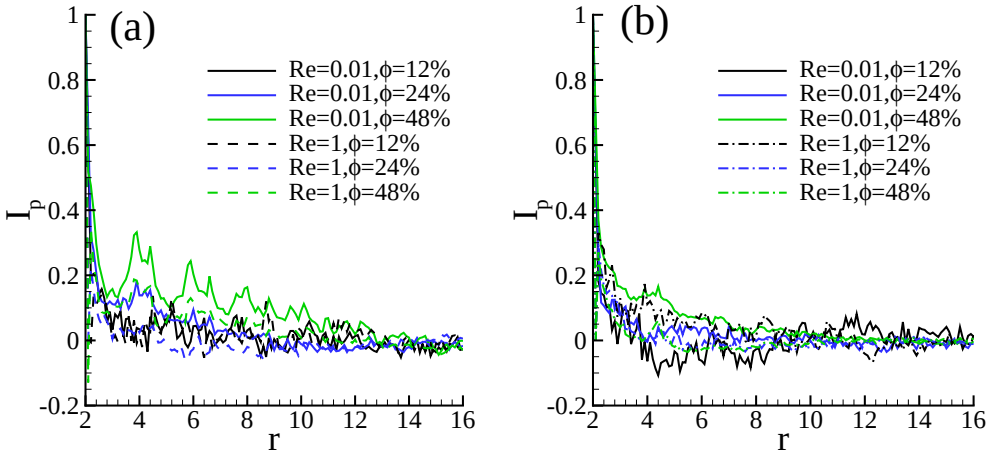

FIG. 7: Particle velocity correlation function I_p at the different concentrations and Re $= 0.01, 1.0$: (a)Puller ($\beta = 3$), (b)Pusher ($\beta = -3$).

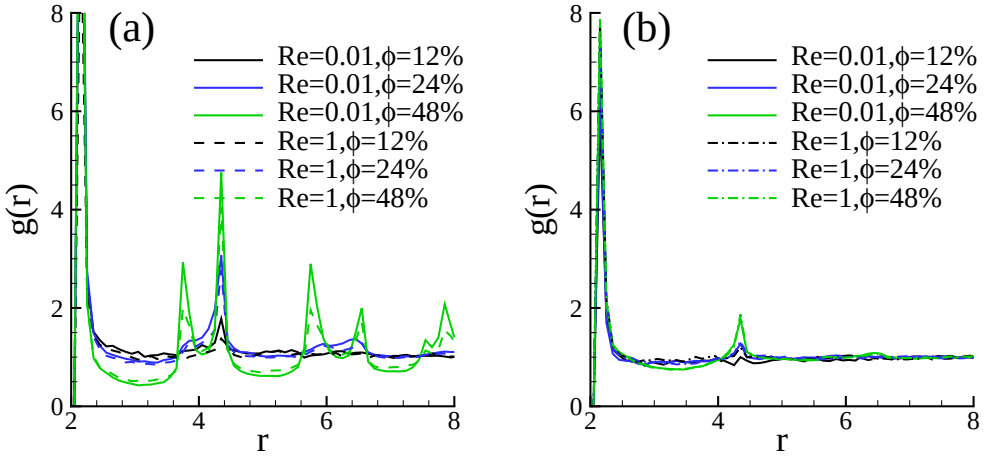

FIG. 8: Pair distribution function $g(r)$ at the different concentrations and Re $= 0.01, 1.0$: (a)Puller ($\beta = 3$), (b)Pusher ($\beta = -3$).

distributions. It is significantly reduced in the dense cases, especially for the Pusher suspension at $\phi = 48\%$ where the two PDFs almost coincide with each other.

As shown in Fig. 10, we combine the results of the time-averaged velocity magnitude for the induced in-plane flows $< \overline{|\mathbf{u}|} >$ and all swimmers $< \overline{|\mathbf{U}_p|} >$ at quasi-steady state. For both Pushers and Pullers, $< \overline{|\mathbf{u}|} >$ grows monotonically as ϕ increases, and can get close to or even be higher than $< \overline{|\mathbf{U}_p|} >$ for the dense cases. Comparing to $< \overline{|\mathbf{u}|} >$, variations of $< \overline{|\mathbf{U}_p|} >$ at different concentrations are much smaller, and only fluctuate around the single swimmer speed as shown by the PDFs in Fig. 9. For the Pusher cases shown in panel(a) of Fig. 10, $< \overline{|\mathbf{U}_p|} >$ are higher at a small Re, and increase monotonically with concentration. For the Pusher cases shown in panel(b), however, $< \overline{|\mathbf{U}_p|} >$ remains approximately to be a constant at a small Re while monotonically decreases with ϕ at a finite Re, again suggesting that the inertia effect gradually diminishes as the particle concentration increases.

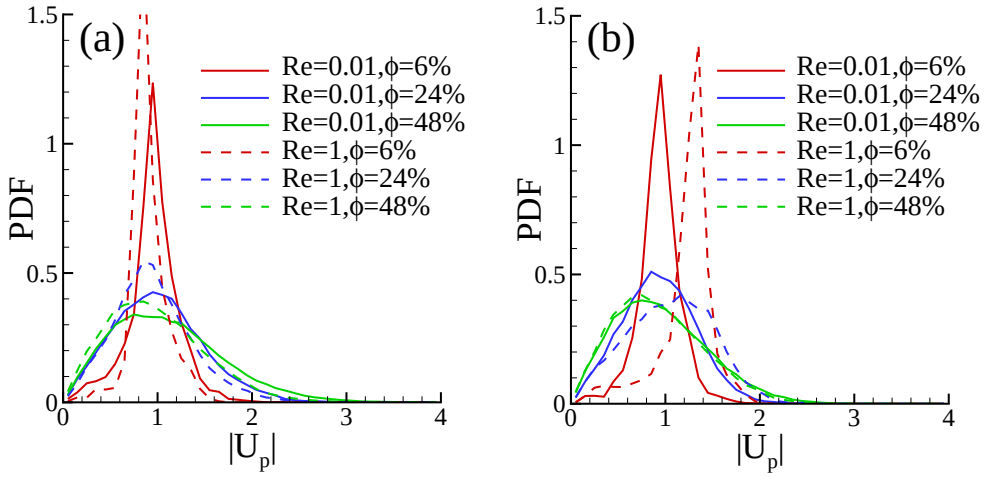

FIG. 9: Probability density functions (PDF) of average speed of the squirmers at the different concentrations and Re $= 0.01, 1.0$: (a)Puller ($\beta = 3$), (b)Pusher ($\beta = -3$).

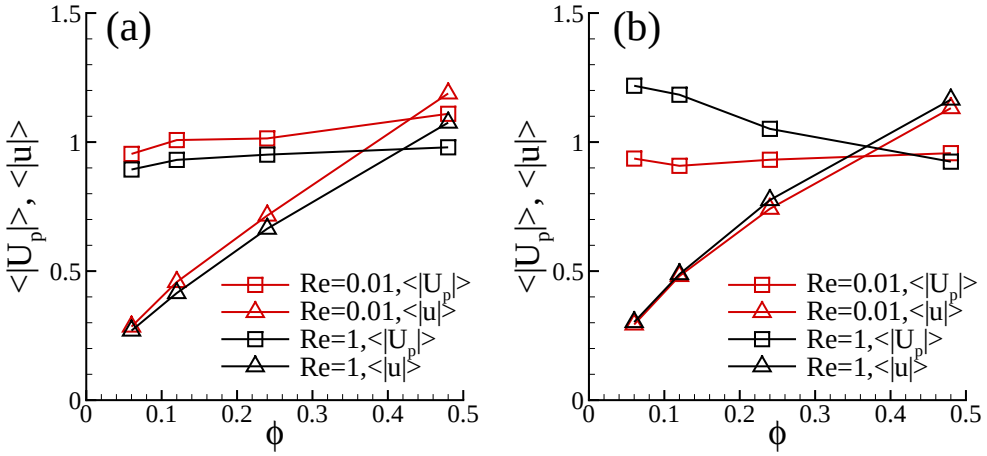

FIG. 10: Average speed of the Squirmers $< \overline{|\mathbf{U}_p|} >$ and the in-plane fluid flow $< \overline{|\mathbf{u}|} >$ computed at the different concentrations and Re $= 0.01, 1.0$: (a)Puller ($\beta = 3$), (b)Pusher ($\beta = -3$).

C. Transport Of Obstacles In Squirmer Monolayer

To further demonstrate our FD method's capability of handling interactions of active particles and geometric boundaries with complex geometries, in this section we study transport behaviors of a large obstacle when placed in the Squirmer monolayer. We expect the obstacle will be driven into motion when simultaneously subject to the viscous forces due to the induced flows and the collision forces arising from contacts with the swimming active particles. This is also inspired by recent experimental studies of active matter systems where self-driven microparticles, when appropriately guided by boundaries, can be used to pump/mix fluids [63–66], cargo transport [67, 68], and power microgears [69]. While strong collective dynamics have been observed for Puller suspensions, however, particle crystallization and the resultant surface flows are unsuitable for obstacle transport. We find that obstacles are usually trapped along the fluid/particle boundaries

instead of being pushed away towards the bulk flow (see an example in Supplemental Movie S1 [70]). Therefore, in the following we focus on the Pusher suspensions at a low Reynolds number (Re = 0.01) where motile particles are well-mixed when interacting collectively.

As sketched in Fig. 11(a), we consider a short cylinder of height $h = 5\Delta x$, and has either a symmetric (circular) or an asymmetric (wedge-like) cross section shape. For the circular cylinder (CC), we set its radius to be $5a$. For the wedge-like cylinder (WC), we set the arm length ℓ to be $10a$ and the thickness w to be $5\Delta x$. (The geometric parameters for WC are selected such that it has the same volume as the Squirmer particle.) Moreover, in the $x-y$ plane, the Lagrangian grid of WC has the same size (Δx) as the Eulerian mesh; while in the $z-$direction, the mesh size is chosen as $5\Delta x/3$ when using three layers in discretization along h. Meanwhile, as described in Section II C, retraction of Lagrangian points from the cylinder surface is enforced. Such Lagrangian grid leads the effective volume ratio (Lagrangian vs. Eularian) about 1.6, which (i.e., the volume ratio between 1 and 2) has been proven to be critical to avoid numerical instabilities [71–73]. The total number of Lagrangian points is between 2500 and 2800, depending on the opening angle γ which determines the shape anisotropy.

The cylinder is initially placed in a monolayer of Pushers with a zero speed. We have performed simulations over a long period of time to track its motion. In Fig. 11, simulation results are compared at $\phi = 12\%, 36\%$ for both shapes. As shown in panel(a), the C.O.M. trajectories of CC at $\phi = 12\%$ and 36% appear to be similar, only drifting around the initial position. On the other hand, in a less-concentrated suspension (i.e., $\phi = 12\%$), noticeably directional migrations characterized by relatively long travel distances (i.e., end-to-end distance) have been observed for WC when varying γ between $\pi/6$ and $2\pi/3$. Here we only show the trajectory for WC with $\gamma = \pi/3$; see Supplemental Movie S2 [70]. For the dense case (i.e., $\phi = 36\%$, see Supplemental Movie S3 [70]), however, WC motion is seemingly to become less directional, similar to those of CC. In panel(b), we compare the corresponding measurements of the mean-square-displacement (MSD). All the cases first exhibit a ballistic behavior in a short time scale. For WC swimming in a less-concentrated monolayer, the MSD remains to be ballistic for a long time $t \approx 100$; while for the other cases, the MSD switches to be diffusive when $t \approx 10$ or even earlier, especially for the case of WC in a dense suspension. As shown in the inset of panel(b), WC's time-averaged migration speed magnitude $< |\mathbf{U}_{cyl}| >$ decreases as γ changes from acute to obtuse. And for each γ, $< |\mathbf{U}_{cyl}| >$ increases as ϕ increases, due to the enhanced particle-particle interactions and more frequent collisions.

The above transport behavior of short cylinder, especially the observed directional migration of WC in a less-concentrated Pusher monolayer, can be further understood by examining the directions of its velocity $\mathbf{U}_{cyl}$, the resultant hydrodynamic ($\mathbf{F}_H$, see Eq. (10)), and collision ($\mathbf{F}_C = \sum_i \sum_{j,i\neq j} \mathbf{f}_{ij}$, see Eq. (4)) forces. As shown in the schematic in Fig. 12(a), we measure the probability distribution of the projected angle p_θ measured from the axis of symmetry in the moving frame fixed on the cylinder during the entire history, with $\theta = \pi$ pointing towards the right-front direction. For the cases of CC shown in Fig. 12(a) and (b), the p_θ distribution for $\mathbf{U}_{cyl}$ suggests that it moves in random directions (at a long time scale), and the migration velocity and the applied forces are uncorrelated. However, in panel(c) where WC moves in a less-concentrated suspension, the p_θ for $\mathbf{U}_{cyl}$ exhibit strong biases in the direction between $\pi/2$ and $3\pi/2$, with two peaks approximately at $\theta = 2\pi/3$ and $\theta = 4\pi/3$. It suggests that the WC tends to move along either the upper-left or upper-right direction relative to its own body axis. Interestingly, the p_θ for $\mathbf{F}_C$ ($\mathbf{F}_H$) appears to be in (or out of) phase with that of $\mathbf{U}_{cyl}$. It can be understood that such directional migration of WC is in fact driven by the (statistically) anisotropic collision force which is balanced by the viscous drag. Similar but much smaller biases are seen for the PDFs in panel(d), corresponding to the case when WC moves in a more concentrated suspension, which, again, is consistent with a

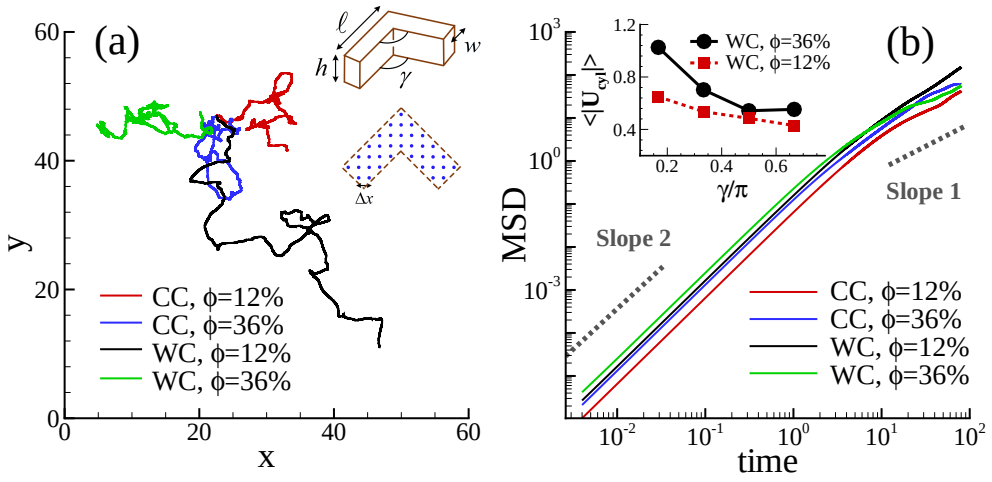

FIG. 11: Comparison of transport of a short circular cylinder (CC) and wedge-like cylinder (WC, $\gamma = \pi/3$) in a Pusher monolayer ($\beta = -3, a = 1.0, \mathrm{Re} = 0.01, \phi = 12\%, 36\%$): (a) Trajectory and (b) MSD. Inset in (a): Schematic for WC as well as the in-plane Lagrangian points distribution. Inset in (b): Mean migration velocity (i.e., C.O.M. velocity) magnitude of WC as a function of γ at two different concentrations.

much weakened directional motion of WC observed in Fig. 11.

In Fig. 13, we reveal the physical mechanism of anisotropic collision force generation by showing the time-averaged density distribution that is centered around the cylinder in the moving body frame. Compared to the cases of CC where the concentration field is nearly homogeneous, for the WC cases, a "hot" area highlighted by the maximum particle concentration robustly occurs near the cusp of the inner surface, which is consistent with the experimental observation by Kaiser *et al.* [67]. As mentioned earlier in Section III A, the Pusher particles tend to stick to and glide along the wall for a certain distance, which facilitates creation of such "trapping zone" near the cusp. Again, such particle accumulation effect near obstacle walls or surfaces is dominated by the local interactions, and has also been observed for active particle systems without hydrodynamic interactions [74]. It becomes prominent (weakened) in less (more) concentrated suspensions where local particle accumulation yields an anisotropic (homogeneous) spatial distribution.

Following the previous studies for Brownian active particles [22, 75, 76], here we seek further quantitative connections between the collision force $\mathbf{F}_C$ and the non-Brownian active particle number density n via a surface integral form:

$$\mathbf{F}_S(t) = -\alpha_0 \int_{\partial C} n(\mathbf{x}, t)\, \mathbf{n} dS \tag{33}$$

where $\mathbf{n}$ is the outer normal of the body surface (∂C), and α_0 is an energy scaling factor (e.g., $\alpha_0 \propto K_B T$ for Brownian particles and $\alpha_0 \propto \mu U_p a^2$ for Squirmer particles considered here). Here we have also simplified our analysis by assuming that the force magnitude $|\mathbf{F}_C|$ is approximately the same for each collision. Corresponding to the cases in Fig. 13(a-d), a highly anisotropic number density distribution with a trapping zone near the cusp facilitates generation of a net forward force. In comparison, while the mean speed of WC in a dense suspension is generally larger, it easily loses direction control due to a more homogeneous number density distribution as the trapping zone fades away as shown in the panels(f-h). To evaluate the directional statistics of $\mathbf{F}_s$, we have numerically computed the surface integral in Eq. (33) (without the unknown coefficient α_0) and shown the corresponding $p(\theta)$ for both CC and WC in Fig. 12 (green solid lines). Not

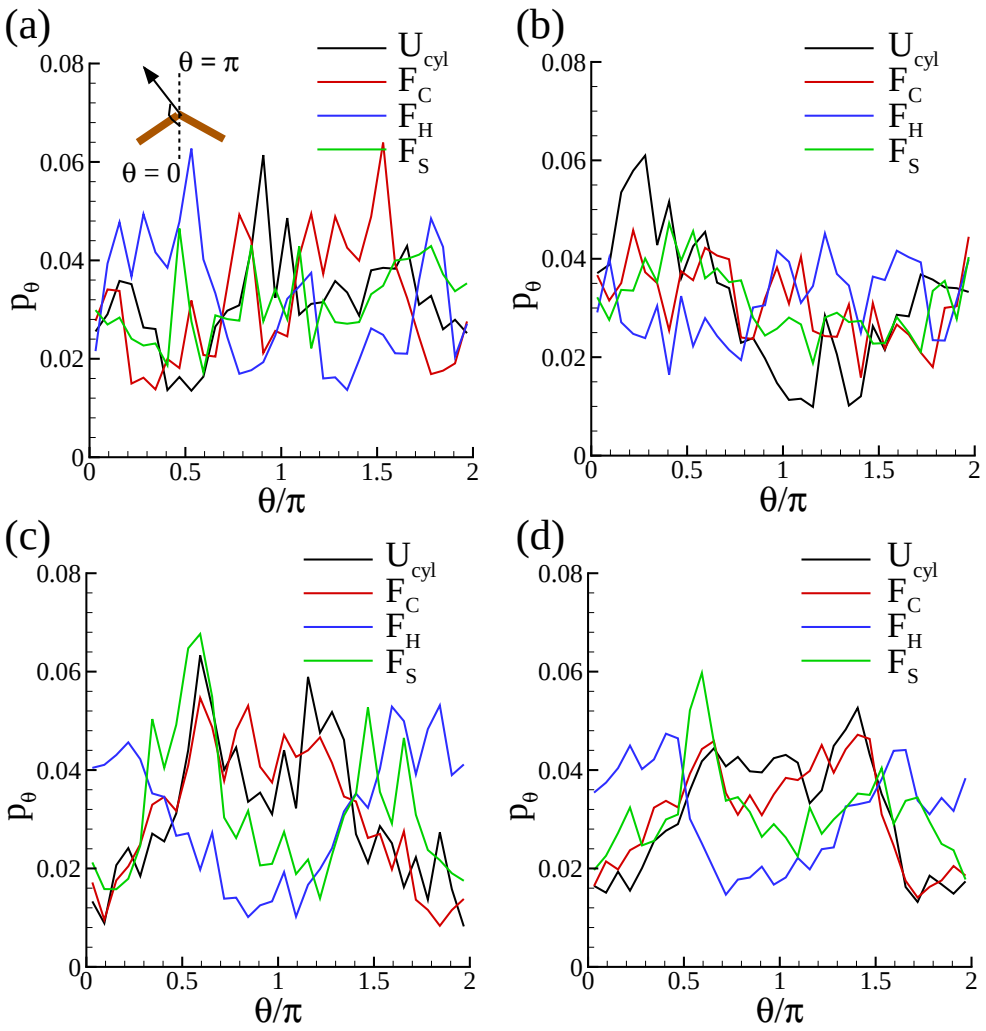

FIG. 12: Orientation probability distribution p_θ for the in-plane migration velocity $\mathbf{U}_{cyl}$, the applied viscous ($\mathbf{F}_H$) and collision ($\mathbf{F}_C$) force, as well as the estimated contact force through a surface integral $\mathbf{F}_S$ (in Eq. (33)) for the cases in Fig. 11: (a, b) CC at $\phi = 12\%, 36\%$; (c, d) WC with $\gamma = \pi/3$ at $\beta = -3, a = 1.0, \mathrm{Re} = 0.01, \phi = 12\%, 36\%$.

surprisingly, while appearing to be more or less uncorrelated for CC in panels(a,b) of Fig. 12, the orientation distribution of $\mathbf{F}_s$ in panels(c,d) approximately follow that of $\mathbf{F}_c$ and $\mathbf{U}_{cyl}$. Therefore, we have confirmed that Eq. (33) reasonably capture the geometrically-dependent nature of the collision-driven process for non-Brownian active particles.

IV. CONCLUSION

In this work we present a direct-forcing fictitious domain method to solve dynamics of non-Brownian Squirmer particles that mimic swimming micro-organisms in the high-activity limit where the advective forces produced by particle activity dominate over random thermal forces. Compared to other similar Cartesian grid methods that often require iterations to achieve convergence [3, 77, 78], this algorithm employs a discrete δ-function to map physical variables between the overlaid Lagrangian and Eulerian meshes, which does not require additional iterations to achieve

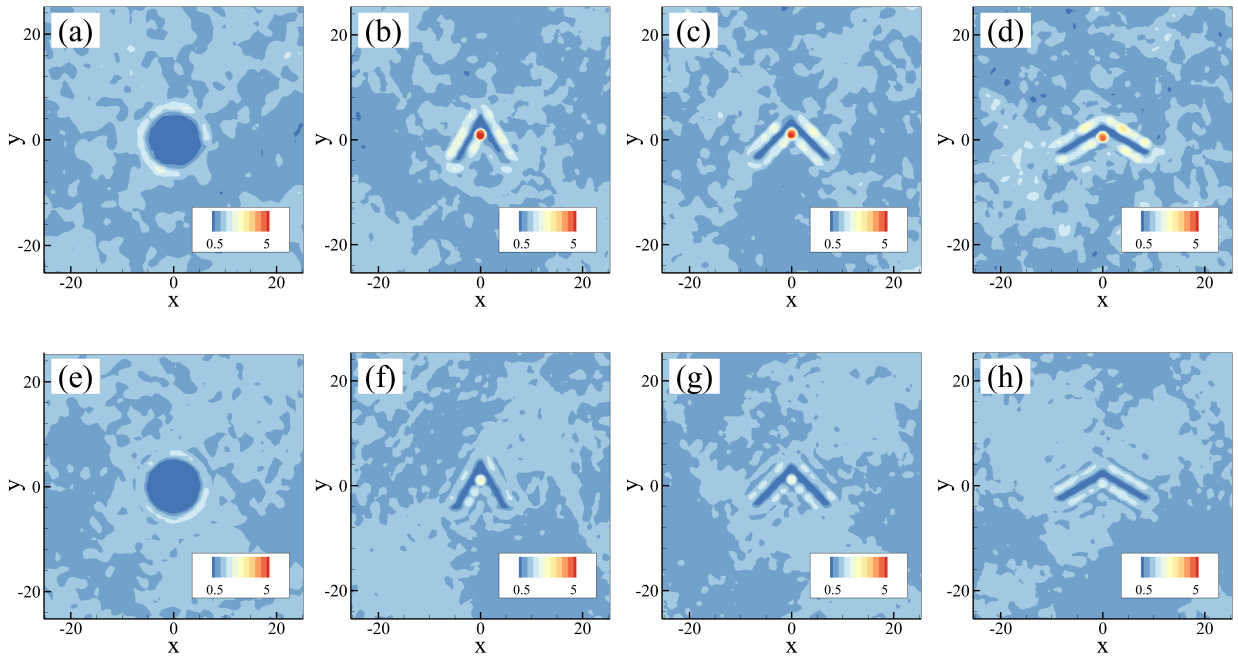

FIG. 13: The time-averaged number density field of Pusher particles ($\beta = -3, a = 1.0, \mathrm{Re} = 0.01$): (a,e) CC at $\phi = 12\%, 36\%$; (b,f) WC with $\gamma = \pi/3$, $\phi = 12\%, 36\%$; (c,g) WC with $\gamma = \pi/2$, $\phi = 12\%, 36\%$; (d,h) WC with $\gamma = 2\pi/3$, $\phi = 12\%, 36\%$.

converged solutions. In addition, an efficient MPI-based parallel algorithm is implemented to speed up computation. We have examined the performance (e.g., accuracy and robustness) of the method through a series of numerical studies at both small and finite Reynolds numbers, and have found excellent agreements with previous studies of free-swimming motion of a single Squirmer and pair interactions between two side-by-side Squirmers.

Since both the hydrodynamic interactions and collisions are fully resolved, we have demonstrated that our method is particularly useful in exploring collective dynamics of active suspensions across Reynolds numbers by measuring detailed statistic properties of a monolayer of confined Pusher particles immersed in a bulk flow. As discussed in Section III B, the enhanced particle-particle interactions in concentrated suspensions lead to emergent coherent quasi-2D structures which can be drastically different for Pullers and Pushers (i.e., phase separation vs. mixing). As Re increases, the collective dynamics for both Pushers and Pullers are seen to be weakened (or less correlated), suggesting that the inertia effect tends to suppress the collective dynamics. More interestingly, as inspired by the experiment by Kaiser *et al.* [67], we have demonstrated that directional motions of short cylinder in the Pusher monolayer is feasible when employing a wedge-like shape. By analyzing the direction correlation between the cylinder's (in-plane) migration velocity and the applied viscous and collision force for long time, we have revealed that transport of cylinder is driven by the resultant collision force due to the shape anisotropic (i.e., wedge-like). As Pusher particles interact with the cylinder collectively, attractive particle-wall interactions lead to a trapping zone with the maximum particle number density near the cusp of the inner surface. Such an inhomogeneous particle distribution along the cylinder surface effectively yields biases of the collision force approximately in the forward direction, especially in a less-concentrated suspension where accumulation of swimming particles near surface is more prominent compared to the dense suspensions. While only a wedge-like shape is studied, the same strategy can be used to design and optimize

geometries for self-driven obstacles to achieve effective migration driven by active suspensions.

Beyond the Squirmer model of a spherical shape, it is straightforward to extend our method to incorporate more elaborate micromechanical models by employing various arrangements of collocation points and active velocity fields in the particle domain, especially for non-spherical particles (ellipsoidal or rod-like) [37, 79, 80]. In general, it is desirable for us to perform fully resolved discrete particle simulations to reveal fascinating coherent structures of various active systems with or without topological confinements at high dimensions, which may suggest novel mechanisms of exploiting anomalous non-equilibrium properties of active matter for useful mechanical work.

Acknowledgments. T.G. acknowledges fruitful discussions with Z. Yu, X. Shao and W. Yan. This work is partially funded by NSF grant DMS-1619960.

[1] S. Ramaswamy. The mechanics and statistics of active matter. Ann. Rev. Cond. Matt. Phys., 323, 1 (2010).
[2] M. C. M. van Loosdrecht, J. Lyklema, W. Norde, and A. J. B. Zehnder. Influence of interfaces on microbial activity. *Microbiol. Rev.*, 54, 75 (1990).
[3] G.J. Li and A. M. Ardekani. Hydrodynamic interaction of micorswimmers near a wall. *Phys. Rev. E*, 90, 013010 (2014).
[4] J. R. Howse, R. A. Jones, A. J. Ryan, T. Gough, R. Vafabakhsh, and R. Golestanian. Self-motile colloidal particles: From directed propulsion to random walk. *Phys. Rev. Lett.*, 99, 048102 (2007).
[5] Y. Sumino, K. H. Nagai, Y. Shitaka, D. Tanaka, K. Yoshikawa, H. Chate, and K. Oiwa. Large-scale vortex lattice emerging from collectively moving microtubules. *Nature (London)*, 483, 448 (2012).
[6] T. Sanchez, D. Chen, S. DeCamp, M. Heymann, and Z. Dogic. Spontaneous motion in hierarchically assembled active matter. *Nature*, 491, 431 (2012).
[7] D. Koch and G. Subramanian. Collective hydrodynamics of swimming microorganisms: living fluids. *Annu. Rev. Fluid Mech.*, 43, 637 (2011).
[8] M. Marchetti, J. Joanny, S. Ramaswamy, T. Liverpool, J. Prost, M. Rao, and R. Simha. Hydrodynamics of soft active matter. *Rev. Mod. Phys.*, 85, 1143 (2013).
[9] D. Saintillan and M. Shelley. Active suspensions and their nonlinear models. *C. R. Phys.*, 14, 497 (2013).
[10] M. Shelley. The dynamics of microtubule/motor-protein assemblies in biology and physics. *Annu. Rev. Fluid Mech.*, 48, 487 (2016).
[11] T. Liverpool and M. Marchetti. Instabilities of isotropic solutions of active polar filaments. *Phys. Rev. Lett.*, 90, 13802 (2003).
[12] C. Wolgemuth. Collective swimming and the dynamics of bacterial turbulence. *Biophys. J.*, 95, 1564 (2008).
[13] D. Saintillan and M. Shelley. Instabilities and pattern formation in active particle suspensions: Kinetic theory and continuum simulations. *Phys. Rev. Lett.*, 100, 178103 (2008).
[14] F. Woodhouse and R. Goldstein. Spontaneous circulation of confined active suspensions. *Phys. Rev. Lett.*, 109, 168105 (2012).
[15] T. Gao, R. Blackwell, M. Glaser, M. Betterton, and M. Shelley. Multiscale polar theory of microtubule and motor-protein assemblies. *Phys. Rev. Lett.*, 114, 048101 (2015).
[16] T. Gao, M. Betterton, A. Jhang, and M. Shelley. Analytical structure, dynamics, and coarse-graining of a kinetic model of an active fluid. *Phys. Rev. Fluids*, 2, 093302 (2017).
[17] T. Gao and Z. Li. Self-driven droplet powered by active nematics. *Phys. Rev. Lett.*, 119, 108002 (2017).
[18] D. Saintillan, E. Darve, and E. Shaqfeh. A smooth particle-mesh ewald algorithm for stokes suspension simulations: The sedimentation of fibers. *Phys. Fluids*, 17, 033301 (2005).
[19] J. W. Swan, J. F. Brady, and R. S. Moore. Modeling hydrodynamic self-propulsion with stokesian dynamics. or teaching stokesian dynamics to swim. *Phys. Fluids*, 23, 071901 (2011).
[20] C. Pozrikidis. *Boundary integral and singularity methods for linearized viscous flow.* Cambridge University Press, 1992.
[21] J. Brady and G. Bossis. Stokesian dynamics. *Annu. Rev. Fluid Mech.*, 20, 111 (1988).

[22] J. Brady. Brownian motion, hydrodynamics, and the osmotic pressure. *J. Chem. Phys.*, 98, 3335 (1993).

[23] S. Lomholt and M. Maxey. Force-coupling method for particulate two-phase flow: Stokes flow. *J. Comput. Phys*, 184, 381 (2003).

[24] J. Keller and S. Rubinow. Slender-body theory for slow viscous flow. *J. Fluid Mech.*, 75, 705 (1976).

[25] G. Batchelor. Slender-body theory for particles of arbitrary cross-section in stokes flow. *J. Fluid Mech.*, 44, 419 (1970).

[26] A. Tornberg and M. Shelley. Simulating the dynamics and interactions of flexible fibers in stokes flows. *J. Comput. Phys*, 196, 8 (2004).

[27] D. Saintillan, E. Darve, and E. Shaqfeh. A smooth particle-mesh ewald algorithm for stokes suspension simulations: The sedimentation of fibers. *Phys. Fluids*, 17, 033301 (2005).

[28] L. Greengard and V. Rokhlin. A fast algorithm for particle simulations. *J. Comput. Phys.*, 73, 325 (1987).

[29] J. Yen. Life in transition: balancing inertial and viscous forces by planktonic copepods. *Biol. Bull.*, 198,213 (2000).

[30] A. Hamel, C. Fisch, L. Combettes, P. Dupuis-Williams, and C. N. Baroud. Transitions between three swimming gaits in paramecium escape. *Proc. Nat. Acad. Sci.*, 108, 7290 (2011).

[31] S. Wang and A. Ardekani. Unsteady swimming of small organisms. *J. Fluid Mech.*, 702, 286 (2012).

[32] S. Wang and A. Ardekani. Inertial squirmer. *Phys. Fluids*, 24, 101902 (2012).

[33] Z. Lin, J. L. Thiffeault, and S. Childress. Stirring by squirmers. *J. Fluid Mech.*, 669, 167 (2011).

[34] B. Thomases and R. Guy. Mechanisms of elastic enhancement and hindrance for finite-length undulatory swimmers in viscoelastic fluids. *Phys. Rev. Lett.*, 113, 098102 (2014).

[35] H. Wu, A. Farutin, W. Hu, M. Thiébaud, S. Rafaï, P. Peyla, M. Lai, and C. Misbah. Amoeboid swimming in a channel. *Soft matter*, 12, 7470 (2016).

[36] G. Li, A. Ostace, and A. Ardekani. Hydrodynamic interaction of swimming organisms in an inertial regime. *Phys. Rev. E*, 94, 053104 (2016).

[37] G.J. Li and A. M. Ardekani. Collective motion of microorganisms in a viscoelastic fluid. *Phys. Rev. Lett.*, 117, 118001 (2016).

[38] Z. S. Yu and X. M. Shao. A direct-forcing fictitious domain method for particulate flows. *J. Comput. Phys.*, 227, 292 (2007).

[39] X. M. Shao, T. H. Wu, and Z. S. Yu. Fully resolved numerical simulation of particle-laden turbulent flow in a horizontal channel at a low reynolds number. *J. Fluid Mech.*, 693, 319 (2012).

[40] X. M. Shao, Y. Shi, and Z. S. Yu. Combination of the fictitious domain method and the sharp interface method for direct numerical simulation of particulate flows with heat transfer. *Int. J. Heat Mass Tran.*, 55, 6775 (2012).

[41] Z. Yu, T. Wu, X. Shao, and J. Lin. Numerical studies of the effects of large neutrally buoyant particles on the flow instability and transition to turbulence in pipe flow. *Phys. Fluids*, 25, 043305 (2013).

[42] Z. Yu, Z. Lin, X. M. Shao, and L. P. Wang. A parallel fictitious domain method for the interface-resolved simulation of particle-laden flows and its application to the turbulent channel flow. *Eng. Appl. Comput. Fluid Mech.*, 10, 160 (2016).

[43] Z. S. Yu Z. W. Lin, X. M. Shao and L. P. Wang. Effects of finite-size heavy particles on the turbulent flows in a square duct. *J. Hydrodyn, Ser. B*, 29, 272 (2017).

[44] M. J. Lighthill. On the squirming motion of nearly spherical deformable bodies through liquids at very small reynolds numbers. *Commun. Pure Appl. Maths*, 5, 109 (1952).

[45] T. Ishikawa and T. Pedley. The rheology of a semi-dilute suspension of swimming model micro-organisms. *J. Fluid Mech.*, 588, 399 (2007).

[46] J. R. Blake. A spherical envelope approach to ciliary propulsion. *J. Fluid Mech.*, 46, 199 (1971).

[47] O. S. Pak and E. Lauga. Generalized squirming motion of a sphere. *J. Eng. Math.*, 8, 1 (2014).

[48] L. Zhu, E. Lauga, and L. Brandt. Low-reynolds-number swimming in a capillary tube. *J. Fluid Mech*, 726, 285 (2013).

[49] A. S. Khair and N. G. Chisholm. Expansions at small reynolds numbers for the locomotion of a spherical squirmer. *Phys. Fluids*, 26, 011902 (2014).

[50] R. Glowinski, T. W. Pan, T. Hesla, and D.D. Joseph. A distributed Lagrange multiplier/fictitious domain method for particulate flows. *Inter. J. Multi. Flow*, 25, 755 (1999).

[51] R. Glowinski, T. W. Pan, T. Hesla, D.D. Joseph, and J. Periaux. A fictitious domain approach to

the direct numerical simulation of incompressible viscous flow past moving rigid bodies: application to particulate flow. *J. Comput. Phys.*, 169, 363 (2001).
[52] R. Mittal and G. Iaccarino. Immersed boundary methods. *Annu. Rev. Fluid Mech.*, 37, 239 (2005).
[53] T. Gao, Y. Tseng, and X. Lu. An improved hybrid cartesian/immersed boundary method for fluidsolid flows. *Int. J. Numer. Meth. Fluids*, 55, 1189 (2007).
[54] N. Chisholm, D. Legendre, E. Lauga, and A. Khair. A squirmer across reynolds numbers. *J. Fluid Mech*, 796, 233 (2016).
[55] T. Ishikawa, M. P. Simmonds, and T. J. Pedley. Hydrodynamic interaction of two swimming model micro-organisms. *J. Fluid Mech.*, 568, 119 (2006).
[56] T. Ishikawa and T. J. Pedley. Coherent structures in monolayers of swimming particles. *Phys. Rev. Lett.*, 100, 088103 (2008).
[57] X. Wu and A. Libchaber. Particle diffusion in a quasi-two-dimensional bacterial bath. *Phys. Rev. Lett.*, 84, 3017 (2000).
[58] J. T. Locsei T. Ishikawa and T. J. Pedley. Development of coherent structures in concentrated suspensions of swimming model micro-organisms. *J. Fluid Mech.*, 615, 401 (2008).
[59] J. Palacci, S. Sacanna, A. Steinberg, D. Pine, and P. Chaikin. Living crystals of light-activated colloidal surfers. *Science*, 339, 936 (2013).
[60] A. Zöttl and H. Stark. Hydrodynamics determines collective motion and phase behavior of active colloids in quasi-two-dimensional confinement. *Phys. Rev. Lett.*, 112, 118101 (2014).
[61] D. Saintillan and M. Shelley. Emergence of coherent structures and large-scale flows in motile suspensions. *J. Roy. Soc. Int.*, 9, 571 (2012).
[62] L. Caprini, U. M. B. Marconi, and A. Puglisi. Activity induced delocalization and freezing in self-propelled systems. *Sci. Rep.*, 9, 1386 (2019).
[63] A. Bricard, J. Caussin, N. Desreumaux, O. Dauchot, and D. Bartolo. Emergence of macroscopic directed motion in populations of motile colloids. *Nature*, 503, 95 (2013).
[64] H. Wioland, F. Woodhouse, J. Dunkel, J. Kessler, and R. Goldstein. Confinement stabilizes a bacterial suspension into a spiral vortex. *Phys. Rev. Lett.*, 110, 268102 (2013).
[65] H. Wioland, E. Lushi, and R. Goldstein. Directed collectivemotion of bacterial under channel confinement. *New J. Phys.*, 18, 075002 (2015).
[66] H. Wioland, F. Woodhouse, J. Dunkel, J. Kessler, and R. Goldstein. Ferromagnetic and antiferromagnetic order in bacterial vortex lattices. *Nat. Phys.*, 12, 341 (2016).
[67] A. Kaiser, A. Peshkov, A. Sokolov, H. B. Ten, H. Löwen, and I. S. Aranson. Transport powered by bacterial turbulence. *Phys. Rev. Lett.*, 112, 158101 (2014).
[68] P.K. Purohit P.E. Arratia A.E. Patteson, A.Gopinath. Particle diffusion in active fluids is non-monotonic in size. *Soft Matter*, 12, 2365 (2016).
[69] A. Sokolov, M. Apodaca, B. Grzybowski, and I. Aranson. Swimming bacteria power microscopic gears. *Proc. Natl. Acad. Sci.*, 107, 969 (2010).
[70] See supplemental material at [url] for movie s1-s3 that show details of swimmer-obstacle interactions.
[71] Z. Yu. A DLM/FD method for fluid/flexible-body interactions. *J. Comput. Phys.*, 207, 1 (2005).
[72] Z. Yu, Y. Wang, and X. Shao. Numerical simulations of the flapping of a three-dimensional flexible plate in uniform flow. *J. Sound Vib.*, 331, 4448 (2012)
[73] Z. Lin, A. Hess, Z. Yu, S. Cai, and T. Gao. A fluid-structure interaction study of soft robotic swimmer using a fictitious domain/active-strain method. *J. Comput. Phys.*, 376, 1138 (2019).
[74] L. Caprini and U. M. B. Marconi. Active particles under confinement and effective force generation among surfaces. *Soft matter*, 14, 9044 (2018).
[75] T. Squires and J. Brady. A simple paradigm for active and nonlinear microrheology. *Phys. Fluids*, 17, 073101 (2005).
[76] W. Yan and J. Brady. The force on a boundary in active matter. *J. Fluid Mech.*, 785, R1 (2015).
[77] N. Sharma and N. A.Patankar. A fast computation technique for the direct numerical simulation of rigid particulate flows. *J. Comput. Phys.*, 205, 439 (2005).
[78] A. Ardekani, S. Dabiri, and R. Rangel. Collision of multi-particle and general shape objects in a viscous fluid. *J. Comput. Phys.*, 227, 10094 (2008).
[79] E. Lushi, H. Wioland, and R. Goldstein. Fluid flows generated by swimming bacteria drive self-organization in confined fluid suspensions. *Proc. Nat. Acad. Sci.*, 111, 9733 (2014).
[80] K. Kyoya, D. Matsunaga, Y. Imai, T. Omori, and T. Ishikawa. Shape matters: Near-field fluid me-

chanics dominate the collective motions of ellipsoidal squirmers. *Phys. Rev. E*, 92, 063027 (2015).